Classical-quantum correspondence in atomic ionization by midinfrared pulses: Multiple peak and interference structures

Christoph Lemell, Joachim Burgdörfer, and Stefanie Gräfe
Institute for Theoretical Physics, Vienna University of Technology, Wiedner Hauptstraße 8-10, A-1040 Vienna, Austria, European Union

Konstantinos I. Dimitriou
Department of Physical Science and Applications, Hellenic Army Academy, Vari, Greece, European Union
and Institute of Theoretical and Chemical Physics, National Hellenic Research Foundation, Athens, Greece, European Union

Diego G. Arbó
Department of Physics FCEN, University of Buenos Aires, Argentina
and Institute for Astronomy and Space Physics, IAFE (Conicet-UBA), CC 67, Suc. 28 (1428) Buenos Aires, Argentina

Xiao-Min Tong
Division of Materials Science, Faculty of Pure and Applied Sciences, and Center for Computatinal Science, University of Tsukuba, 1-1-1 Tennodai, Tsukuba, Ibaraki 305-8577, Japan
(Received 30 November 2012; published 22 January 2013)

Atomic ionization by strong and ultrashort laser pulses with frequencies in the midinfrared spectral region have revealed novel features such as the low-energy structures. We have performed fully three-dimensional quantum dynamical as well as classical trajectory Monte Carlo simulations for pulses with wavelengths from $\lambda = 2000$ to 6000 nm. Furthermore, we apply distorted-wave quantum approximations. This allows to explore the quantum-classical correspondence as well as the (non) perturbative character of the ionization dynamics driven by long-wavelength pulses. We observe surprisingly rich structures in the differential energy and angular momentum distribution which sensitively depend on λ, the pulse duration τ_p, and the carrier-envelope phase ϕ_{CEP}.

DOI: 10.1103/PhysRevA.87.013421 PACS number(s): 32.80.Rm, 34.80.Qb, 32.80.Fb

I. INTRODUCTION

Many strong-field phenomena appearing in atomic and molecular ionization by intense laser fields are explained within the framework of the strong-field approximation (SFA) [1–4]. In this approximation, the motion of an electron after ionization is assumed to be influenced by the electric field of the laser pulse only. The Coulomb field of the ionized atom is neglected as it quickly decreases with increasing distance of the electron from the ion. Especially in the tunneling field regime as characterized by the Keldysh parameter [2] $\gamma = \sqrt{I_p/2U_p} \ll 1$ (where I_p is the ionization potential of the atom, $U_p = F_0^2/4\omega^2$ the ponderomotive energy, F_0 the maximum field amplitude, and ω the central laser frequency), the influence of the Coulomb (atomic) potential on the ionization process is expected to be of vanishing importance.

It thus came as an "ionization surprise" [5] that in the tunnel regime an unexpected structure in the electron-energy spectrum was observed at small energies, which could not be explained within the SFA but could be seen in full quantum mechanical [6–10] and also classical calculations [7,11,12]. Later, the origin of the low-energy structure (LES) was analyzed in detail and was shown to be a largely classical effect of the combined laser and Coulomb fields on the electronic motion after ionization. More recently, it was shown that the formation of the LES is due to a bunching or focusing of electrons during "soft recollisions" [13,14]. At turning points of the quiver motion of the electron in the vicinity of the ionic core ($z \sim 0$ in combination with momentum $p_\parallel \sim 0$), the Coulomb field becomes the dominating (attractive) force acting on the electron. There the electron may lock onto Kepler hyperbolae with well-defined angular momenta L determined by the laser parameters [14]. Subsequently, the electron follows a classical quiver motion centered around the Kepler hyperbola [14,15].

The aim of the present paper is to explore the classical-quantum correspondence for midinfrared pulse-driven electronic dynamics. A starting point is the observation that with increasing λ or, equivalently, decreasing frequency ω, the characteristic excursion distance (quiver amplitude) $\alpha = F_0/\omega^2$ becomes large compared to the "thickness" of the tunnel barrier z_t, $\alpha \gg z_t$. The latter provides one length scale of nonclassical effects. Moreover, the energy absorption in the midinfrared field $\sim U_p$ becomes large compared to the quantum of energy transfer $\sim\hbar\omega$, reaching easily several thousand quanta [16]. In this regime, the dynamics is expected to approach the (semi) classical limit supporting the application of classical models. Nevertheless, even in this regime strong interference, i.e., nonclassical effects ubiquitously persist. Therefore, the classical limit may emerge only upon "coarse graining," for example, by averaging over the focal volume of the laser beam in the experiment.

The outline of this paper is as follows: In Sec. II we briefly review the quantum and classical methods employed. Numerical results will be presented in Sec. III, where we focus on the dependence of the low-energy spectrum on the wavelength λ and pulse duration τ_p. We address the role of multiple scattering as a function of wavelength in the midinfrared

and show that for longer wavelengths multiple low-energy peaks appear which are well separated in energy and angular momentum. These peaks should become observable in the experiment provided that intensity averaging over the focal volume can be controlled. Concluding remarks are given in Sec. IV.

Atomic units are used unless otherwise stated.

II. THEORETICAL METHODS

As a prototypical case we consider a hydrogen atom interacting with short laser pulses with central wavelengths $\lambda = 2$ to 6 μm corresponding to frequencies $\omega \approx 0.023$ to 0.0076 a.u. The total Hamiltonian of this system is given in the dipole approximation by

$$H(t) = \frac{\vec{p}^2}{2} - \frac{Z}{|\vec{r}|} + zF(t), \tag{1}$$

where $\vec{p}$ and $\vec{r}$ are the electron momentum and position, Z is the atomic charge ($Z = 1$ for hydrogen), and the last term of Eq. (1) is the interaction term in the length gauge for an electric field $F(t)$ linearly polarized along the z direction. We derive the electric field $F(t)$ from the vector potential

$$A(t) = A_0 \sin(\omega t + \phi_{\rm CEP}) f_{\rm env}(t), \tag{2}$$

where we use an envelope function $f_{\rm env}(t)$ of $\sin^2(\pi t/\tau_p)$ with τ_p the *total* pulse duration. This ensures that all pulses satisfy the condition $\int_0^{\tau_p} F(t)\,dt = 0$. In the following, τ_p will be given in number of cycles (e.g., one cycle at $\lambda = 3600$ nm takes 12 fs) as the cycle number plays a key role for rescattering. The pulse duration in the experiment as given by its full width at half maximum of the pulse intensity is related to τ_p by $\tau_{\rm exp} \approx 0.364\,\tau_p$.

A. Quantum-mechanical simulation

The full three-dimensional (3D) quantum-mechanical simulation proceeds by discretization of the radial coordinate space in a pseudospectral grid and propagation of the wave function within a finite box by the split-operator method in the energy representation [17] in the time-integral form [18]. In view of the large quiver distance α for midinfrared pulses, particular attention must be paid to the appropriate box size and the prevention of unphysical reflections from the boundary. We therefore separate the real space into an inner ($R < R_c$) and an outer region ($R_c < R < R_{\rm max}$). We propagate the time-dependent wave function within the box and project the wave function in the outer region onto the atomic continuum states. The atomic continuum states are further propagated analytically as Volkov states in momentum space. The criteria for choosing the boundary R_c are that (1) the electron parent-core interaction is negligible and (2) R_c should be much larger than the quiver distance, $R_c \gg \alpha$, so the electron in the outer region cannot return to the vicinity of the parent core. In the present simulation, we choose a total box size of $R_{\rm max} = 800$ a.u. and $R_c = 500$ a.u. which is about 4 times larger than the quiver distance. We use about 4000 radial grid points and 300 partial waves. The numerical convergence is checked by varying the simulation parameters.

B. The Coulomb-Volkov approximation

Ionization by strong fields is frequently treated within the framework of variants of the strong-field distorted wave Born approximation (DWBA). Accordingly, the initial state is governed by the atomic Coulomb field neglecting the laser field while the final state is assumed to be a continuum electron distorted by the strong laser field. Within the DWBA, the transition amplitude in the *post* form is expressed as [19]

$$T_{if} = -i \int_{-\infty}^{+\infty} dt\, \langle \chi_f^-(t)|z\,F(t)\,|\phi_i(t)\rangle\,, \tag{3}$$

where $\phi_i(t)$ is the atomic initial state with binding energy $-I_p$ and $\chi_f^-(t)$ is the final distorted-wave function of the continuum electron. If we choose the Hamiltonian of a free electron in the time-dependent electric field as the exit-channel Hamiltonian neglecting the Coulomb potential altogether, i.e., $i\frac{\partial}{\partial t}|\chi_f^-(t)\rangle = (\frac{p^2}{2} + z\,F(t))|\chi_f^-(t)\rangle$, the solutions are the Volkov states [20]

$$\chi_{\vec{k}}^{(V)-}(\vec{r},t) = \frac{\exp\left[i(\vec{k}+\vec{A})\vec{r}\right]}{(2\pi)^{3/2}} \exp\left[i\,S(t)\right]\,, \tag{4}$$

where S denotes the Volkov action

$$S(t',t) = -\int_{t'}^{t} dt'' \left\{ \frac{[\vec{k}+\vec{A}(t'')]^2}{2} + I_p \right\}. \tag{5}$$

In Eq. (4), $S(t)$ is understood as the action defined in Eq. (5) for the case of $t' \to -\infty$. In Eqs. (4) and (5), $\vec{A}(t)$ is the vector potential of the laser field [Eq. (2)] divided by the speed of light. Equation (3) together with Eq. (4) represents the SFA transition matrix element. Accordingly, since the influence of the atomic core potential on the continuum state of the receding electron is neglected, the momentum distribution is a constant of motion after conclusion of the laser pulse. It is well known that the SFA fails to describe ionization for moderately weak fields as well as the low-energy spectrum even for strong fields [21].

A useful variant of the DWBA is to combine the wave function for a free electron in the laser field with the continuum wave function for the electron in the Coulomb field. For a hydrogenic atom, i.e., $V(r) = -Z/r$ with Z the nucleus charge, this results in the Coulomb-Volkov final state

$$\chi_{\vec{k}}^{(CV)-}(\vec{r},t) = \chi_{\vec{k}}^{(V)-}(\vec{r},t)\mathcal{D}_C(Z,\vec{k},\vec{r}) \tag{6}$$

with the Coulomb state

$$\mathcal{D}_C(Z,\vec{k},\vec{r}) = C\;{}_1F_1(-iZ/k,1,-ikr-i\vec{k}\vec{r})\,, \tag{7}$$

where C is a normalization constant and ${}_1F_1$ the confluent hypergeometric function. Inserting Eq. (6) into Eq. (3) yields the Coulomb-Volkov approximation (CVA). We note that Eq. (7) can be further approximated by reducing the ${}_1F_1$ by its limit for asymptotically large r reducing it to the Coulomb eikonal phase. In this case, Eq. (6) would reduce to the eikonal approximation. It is worth noting that the influence of Coulomb and laser fields are included in Eq. (6) to all orders, however, in factorized form. Expressed in terms of a diagrammatic expansion the latter implies that higher order "mixed" diagrams where interaction vertices with the Coulomb and laser fields alternate are missing. As will

be discussed below, this restriction imposes limitations for describing rescattering.

C. The quasiclassical method

In the strong-field regime ($\gamma < 1$) ionization is frequently described within a quasiclassical approach [22]. After tunneling ionization, the liberated electron follows a classical trajectory in the combined Coulomb and laser fields. As this method is nonperturbative, final-state interactions are fully included. However, quantum interference effects are neglected from the outset. The role of classical trajectories is of interest (from the viewpoint of quantum-classical correspondence) for large λ driving fields.

Our classical trajectory Monte Carlo method with tunneling (CTMC-T) employs an adaptive step size fourth order Runge-Kutta method for the numerical integration of the electron's classical equation of motion [23]. Here we neglect the electron dynamics before tunneling and start the simulation at the tunnel exit. We have checked that this additional approximation alters neither the results of the simulation nor their interpretation, but it provides a faster computational scheme for low-frequency multicycle laser pulses. We chose the initial conditions of each trajectory according to the Delone-Krainov expressions for tunneling probability, position, and momentum [24]. The initial energy of the electron is equal to the energy of the ground state, $-I_p = -0.5$ a.u. for hydrogen. The starting point of the trajectory calculation is determined by the randomly chosen ionization time t_0 and is given by $x_0(t_0) = y_0(t_0) = 0$ and the coordinate of the tunnel exit

$$|z_0(t_0)| = \frac{I_p/F(t_0) + \sqrt{[I_p/F(t_0)]^2 - 4/F(t_0)}}{2}. \quad (8)$$

Since the tunneling probability

$$P_{\mathrm{DK}}(t_0) = \int_0^{t_0} W_{\mathrm{DK}}(t)\,dt \quad (9)$$

with W_{DK} the Delone and Krainov rate [24] may become large for multicycle pulses we take depletion into account in our CTMC simulation. Thus, the effective tunneling probability is reduced to

$$P_{\mathrm{tun}}(t_0) = P_{\mathrm{DK}}(t_0) e^{-\int_0^{t_0} W_{\mathrm{DK}}(t)\,dt}. \quad (10)$$

The initial parallel and perpendicular momentum distributions are Gaussians with widths taken from Ref. [24].

We numerically follow typically 10^6 trajectories from the moment of ionization until the end of the pulse. Only trajectories with final energies $E_{\mathrm{f}} > 0$ are explicitly considered in the following. Their asymptotic momenta are calculated analytically by propagation along Kepler orbits [23].

III. RESULTS

A. Comparison of two-dimensional distributions

We first compare and contrast two-dimensional distributions of emitted electrons predicted by quantum and classical descriptions as well as perturbation theory for both the momentum plane $(p_\parallel, p_\perp)$ parallel and perpendicular to the laser polarization axis and the (E, L) energy-angular momentum plane.

We start with a comparison of the momentum distributions calculated using all three methods described above (Fig. 1) for hydrogen atoms interacting with short midinfrared laser pulses (wavelength $\lambda = 3200$ nm, intensity $I = 10^{14}$ W/cm^2, total pulse duration $\tau_p = 8$ cycles ≈ 85 fs).

The solution of the time-dependent Schrödinger equation (middle panel) displays a remarkably rich structure of features closely associated with quantum interferences thus defying, at first glance, the notion of approaching the classical limit. Prominently visible are the concentric above-threshold ionization (ATI) rings centered around the origin in momentum space. Less well known are the remnants of additional rings due to intracycle interferences centered at $k_z^{\max} = \pm F_0/\omega$

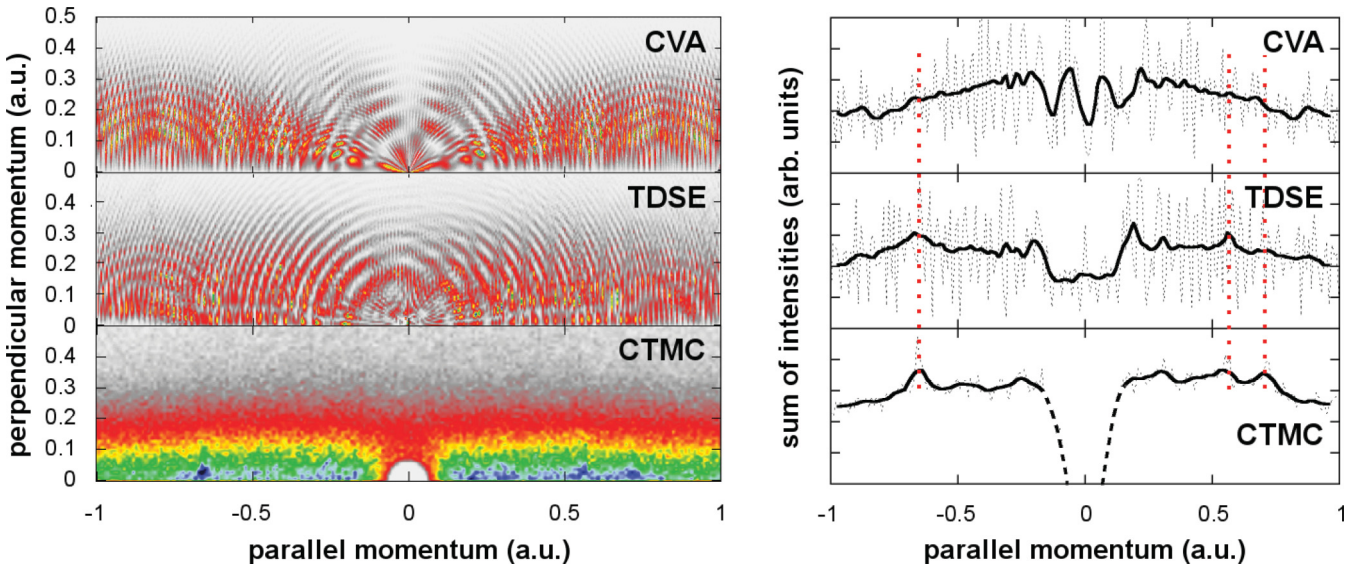

FIG. 1. (Color online) Momentum distributions (linear color scale) after interaction of a strong ($I = 10^{14}$ W/cm^2) midinfrared ($\lambda = 3200$ nm) laser pulse with a hydrogen atom. The distributions were calculated using the CVA (top), full quantum simulation (middle), and CTMC (bottom); the total pulse duration is eight cycles. Left: two-dimensional distributions; right: projection onto $p_\parallel$.

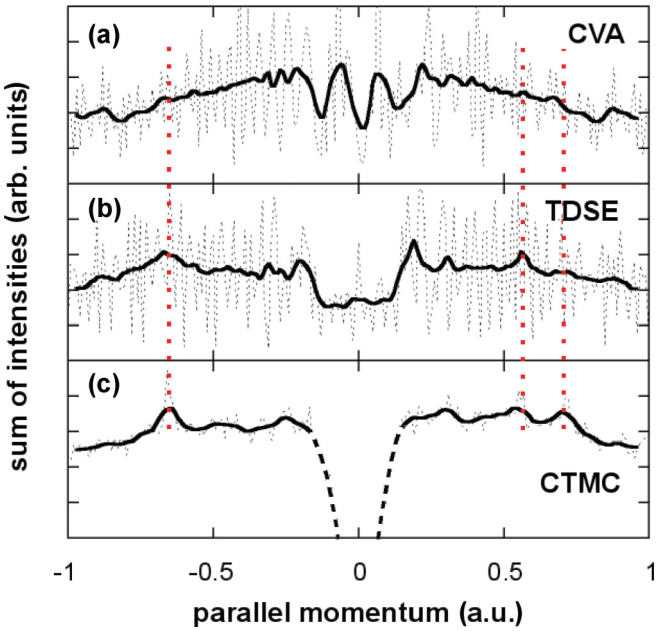

FIG. 2. (Color online) Projected longitudinal momentum distributions averaged over $p_\perp < 0.1$ a.u. Thin lines: $P(p_\parallel)$, thick lines: smoothed distributions $\bar{P}(p_\parallel)$ (average over one oscillation). The position of the LES is indicated by red dotted lines.

[21,25,26]. They are visible, e.g., in Fig. 1(b) near $p_\parallel \approx \pm 1$ a.u. as contour lines bending outward rather than inward. These additional interference structures become only clearly discernible for large F_0/ω and, hence, are more prominently visible for midinfrared pulses. In the present case $F_0/\omega \approx 3.75$ a.u. ($F_0 \approx 0.053$ a.u., $\omega \approx 0.014$ a.u.). Both overlapping ring structures show up also in the CVA distribution (top panel) indicating that these interferences are well represented by perturbation theory. By contrast, the CTMC distribution is smooth, as expected. However, by averaging, i.e. "coarse graining," an approximate classical-quantum correspondence begins to emerge. The projected and smoothed momentum distributions $\bar{P}(p_\parallel)$ along the polarization axis with $p_\perp < 0.1$ a.u. (Fig. 2) display peaks in both forward and backward directions. These structures are clearly visible in the full quantum simulation [Fig. 2(b)] and classical simulation [Fig. 2(c)]. In the CVA [Fig. 2(a)] a weak double-hump structure is visible. The latter is, however, forward-backward symmetric ($\pm p_\parallel$) pointing to another origin, i.e., remnants of constructive inter- and intracycle interference fringes. The peaks visible in both the TDSE and CTMC show a clear forward-backward asymmetry for short pulses. These peaks represent the LESs. Due to the short pulse length, ionization is concentrated to the central half cycle of the cosine-pulse (LES maximum to the left at $p_\parallel \approx -0.64$ a.u.) and its two neighboring half cycles (maxima at $p_\parallel \approx 0.56$ a.u. and 0.72 a.u. to the right). Both the forward-backward differences as well as the multiple peaks are signatures of few-cycle pulses and are sensitive to the carrier-envelope phase $\phi_{\rm CEP}$ [14,27]. The suppression of LES in the CVA underlines the fact that these structures are due to nonperturbative processes in the combined Coulomb and laser fields not fully accounted for by Eq. (7).

Another characteristic feature of the LES is its high angular momentum content [14]. Electrons contributing to the LES are focused near specific values of the final energy E and the angular momentum L. It is therefore instructive to also compare the two-dimensional $E - L$ distributions predicted by the three approaches (Fig. 3). On a fine scale, the CVA shares with the quantum simulation several features such as maxima at multiples of the photon energy and a distance

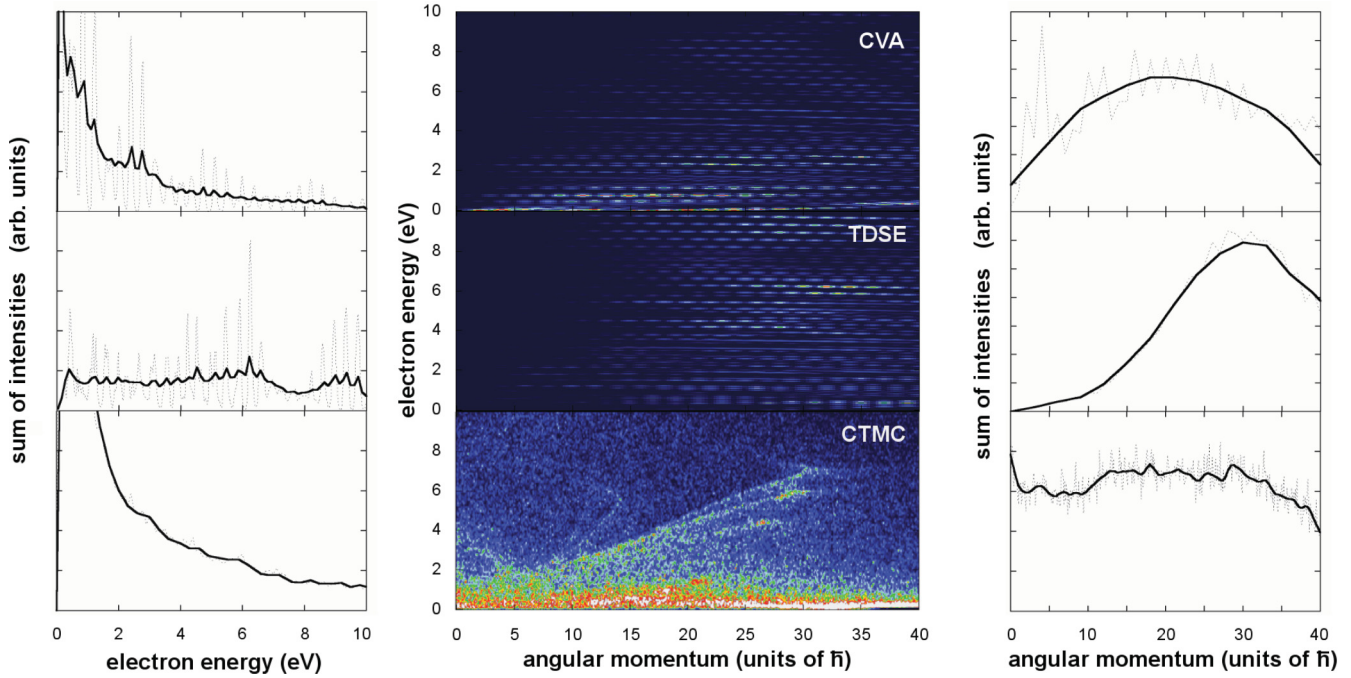

FIG. 3. (Color online) Center: $E - L$ distributions calculated using the CVA (top), TDSE (middle), and CTMC (bottom); projections onto the energy (left) and angular momentum axes (right). To improve contrast a nonlinear color coding ($\sqrt{P(E,L)}$) has been used. Laser parameters as in Fig. 1.

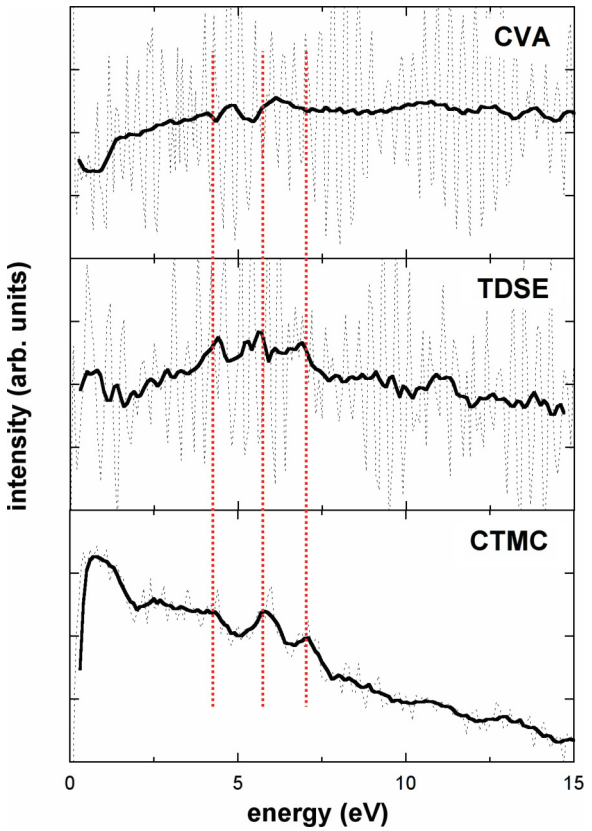

FIG. 4. (Color online) Energy spectra (thin dashed lines) and smoothed energy spectra (average over $\hbar\omega$; thick lines) calculated using the CVA (top panel), TDSE (middle panel), and the CTMC (bottom panel) simulations. The position of the LES is indicated by the red dotted lines (see Fig. 2). Laser parameters as in Fig. 1.

of $\Delta L = 2$ between neighboring peaks in L due to parity-favored transitions, completely absent in the CTMC. Upon coarse graining the comparison changes: the local maximum in the TDSE distribution showing a dramatic shift to high values of L coincides with the broad feature in the CTMC distribution, which is associated with the LES. Such maxima are absent in the CVA, which has its dominant contributions at smaller energies and smaller angular momenta. The energy spectra (Fig. 4) for emission into a forward and backward cone (opening angle $\theta = 10^\circ$) display the LES present in the classical and quantum simulations but not discernible in the CVA. Both the CTMC and the TDSE feature three humps between 4 and 7.5 eV at the energies derived from the positions of the maxima of the momentum distributions in Fig. 2.

B. Origin of the LES: Recollision and focusing in the Coulomb field

As the LES is, at least on a qualitative level, described by the CTMC method, it is instructive to inquire into underlying processes using the full phase space information available from classical trajectories. To simplify the trajectory analysis (Fig. 5) we restrict ionization to the half cycle with maximum field strength of a cosine-like pulse (i.e., $\phi_{\mathrm{CEP}} = 0$) with a $\sin^2$

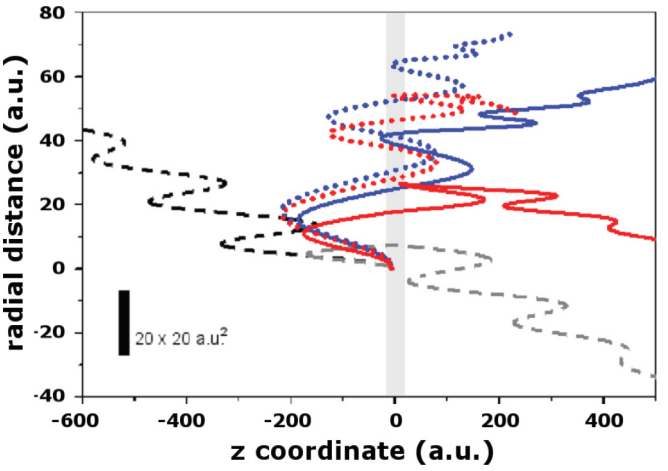

FIG. 5. (Color online) Selected classical trajectories with asymptotic energies in the LES: colored (solid and dotted) trajectories receive a kick in angular momentum at their turning points close to $z = 0$ and are focused into the high-L peak (see Fig. 6). Gray-scale (dashed) trajectories end up at lower L. Note the different scales parallel (z) and perpendicular to the laser polarization axis; a square with 20 a.u. side length is represented by the black box. Laser wavelength $\lambda = 2200$ nm, $\sin^2$ envelope, $\phi_{\mathrm{CEP}} = 0$ corresponding to a cosine-like pulse with pulse duration of eight cycles.

field envelope and intensity $I = 10^{14}$ W/cm^2. The wavelength is $\lambda = 2200$ nm, the total pulse duration eight cycles.

Several classes of trajectories have been discussed in literature in terms of the quadrant in the trajectory plane in which the electron is emitted [7]. In fact, the distinguishing

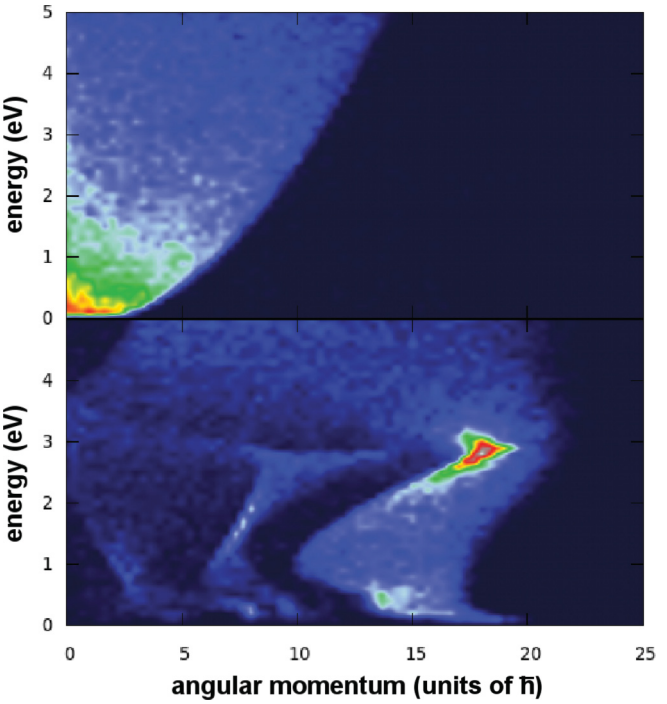

FIG. 6. (Color online) $E - L$ distributions for electrons emitted during the central half cycle of a 10-cycle 2200 nm pulse with $I = 10^{14}$ W/cm^2. The observation direction is along the polarization axis with an opening angle of $\theta_c = \pm 10^\circ$ in forward (top panel) and backward (bottom panel) directions with respect to the tunneling exit.

feature of trajectories contributing to the LES is the location of a (the) turning point: those with turning points close to the $z = 0$ plane and those where the turning points are at larger $|z|$ (Fig. 5). In the former case, the momentum kick imparted by the Coulomb potential shifts the angular momentum towards higher L but transfers only a small amount of energy; in the latter case the situation is reversed. A similar scenario applies to Rydberg atoms for which the optimized timing of "kicks" allows steering wave packets in either high L or high-eccentricity orbits [28]. The turning point near the $z = 0$ plane is not necessarily the one during the first quiver oscillation (Fig. 6) but can also be reached during subsequent oscillations. The latter case gives rise to higher order LES peaks [27,29].

The focusing of electrons can be conveniently monitored as a function of λ and the pulse duration in the $E - L$ plane. The $E - L$ distributions resulting from the CTMC calculations for electron trajectories emitted in forward and backward directions with respect to the tunneling exit, representative examples of which were presented in Fig. 5, are shown in Fig. 6. Trajectories emitted in forward direction, i.e., in the direction of the tunneling exit (represented by the black dashed line in Fig. 5) end up in a featureless background (upper panel in Fig. 6) delimited by the relation

$$E = \frac{L^2}{2\alpha^2 \sin^2 \theta_c}. \tag{11}$$

In contrast, electrons that undergo soft rescattering with a turning point ($p_\parallel = 0$) close to the $z = 0$ plane receive a kick towards larger angular momenta. The subset of trajectories receiving the kicks exactly opposite to their direction of motion, i.e., the Coulomb force acting on the electron has only a radial component ($z \approx 0$, $\Delta p_\perp/\Delta t = F_\perp \approx F_{\text{total}}$), are focused into the LES peak at $E \approx 3$ eV and $L \approx 18$. At small energies ($E \approx 0.5$ eV) and $L \approx 13$ a second order LES peak starts to emerge originating from trajectories receiving their focusing kick at larger radial distances from the nucleus, i.e., at the end of their second quiver oscillation (dotted trajectories in Fig. 5). For such a secondary structure to appear a minimum pulse duration is required in order to drive the electron back to the nucleus one more time.

This observation implies that the LES structures should sensitively depend on λ and on the pulse duration. As shown in Fig. 7, increasing the wavelength to $\lambda = 3200$ nm increases the visibility of the soft recollision processes since their energies scale as $E \propto \gamma^{-2} \propto \lambda^2$. For the $E - L$ distributions for 6, 10, 14, and 30 cycles total pulse length we, again, restrict, for clarity, ionization to the central half cycle of the cosine pulse. LES peaks due to a two-dimensional focusing appear in the $E - L$ plane at the minimal pulse duration for their first appearance [e.g., the $k = 1$ peak for a pulse length of six cycles, Fig. 7(a)] near [14]

$$E_k \approx \frac{8}{(2k+1)^2\pi^2} \frac{F_{0,k}^2}{4\omega^2}, \tag{12}$$

$$L_k \approx p_\perp(t_0)\alpha_{0,k}, \tag{13}$$

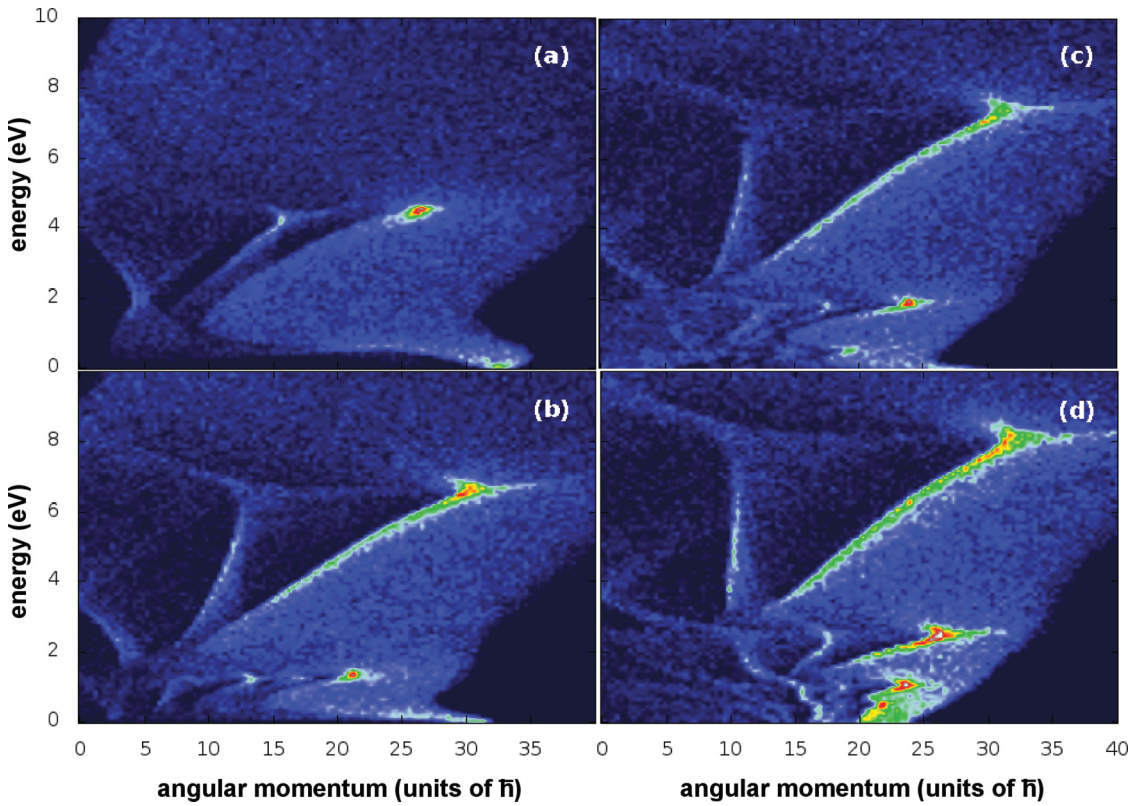

FIG. 7. (Color online) $E - L$ distributions for 3200 nm laser pulses and a peak intensity of $I = 10^{14}$ W/cm^2 interacting with hydrogen. The total pulse lengths are 6 (a), 10 (b), 14 (c), and 30 cycles (d). The appearance of higher order LES peaks as a function of pulse length is observed.

where k is the order of the LES, $p_\perp(t_0)$ is the perpendicular momentum at the time of ionization, and $F_{0,k}(t_k) = F(t_0 + 2\pi[k + 1/2]/\omega)$ and $\alpha_{0,k} = F_{0,k}/\omega^2$ are the field strength and the quiver amplitude at the time of locking t_k onto highly eccentric Coulomb (C) orbits with $L_k \sim L_C$ and $E_k \sim E_C$. It is worth noting that the major axis of the Coulomb hyperbola is strongly tilted with respect to the polarization axis of the laser field as the large eccentricity $\varepsilon = \sqrt{1 + 2EL^2}$ [$\sim$14.5 for the case shown in Fig. 7(a)] implies an opening angle of the asymptote relative to the major axis of $\theta = \arctan\sqrt{\varepsilon^2 - 1} \sim 86^\circ$ [30,31]. For LES electrons focused along the polarization axis of the laser field [14] θ is also close to the tilt angle of the major axis relative to the polarization axis.

Equations (12) and (13) provide accurate estimates for long pulses where many half cycles contribute to the first order LES with slightly different field strengths $F_{0,k}$ [local maxima in first order LES of Fig. 7(d)]. For short pulses [e.g., six cycles in Fig. 7(a)] Eq. (12) is a lower bound for the position of the LES due to the large gradient of the field envelope at locking time. The upper limit for E ("high energy cutoff" $E_{\rm cut}$ [6]) is found by inserting the maximum field amplitude into Eq. (12) [here $\sim$8.6 eV close to the maximum energy of the arch-like structure in Fig. 7(d)].

For longer pulses, higher order peaks appear in accordance with Eqs. (12) and (13). For 14 cycles total pulse length, a third order LES emerges at $E \approx 0.5$ eV. For the longest pulse shown here (30 cycles total pulse length with $\tau_p \approx 320$ fs) the third-order LES attains the largest absolute peak height. The latter is to be distinguished from the larger total intensity spread over the arch-shaped structures for the lower-order peaks. At very small energies LES of order 4 to 6 begin to appear. Very recently, a "very low-energy structure" appearing at energies below 1 eV was experimentally observed ($\lambda = 1320$ and 1800 nm; [32]).

The first-order peak in the $E - L$ plane has been shown to result from a focusing [14] of the initial conditions in the plane of tunneling time $t_{0,k}$ and transverse momentum $p_{\perp,0}$, expressed by the classical transition probability [33,34]. We demonstrate here that this focusing mechanism applies to the entire hierarchy of LES peaks (Fig. 8). The distributions pertain to a total pulse length of 14 cycles [Fig. 7(c)]. We set $p_{\parallel,0} = 0$ to confine the phase space to two dimensions. Only those initial conditions are shown in Fig. 8(b) that correspond to the peaks in the $E - L$ plane [white rectangles in Fig. 8(a)]. The first order LES is due to electron emission at a tunneling time shortly after the maximum of the laser field, while the two additional islands are very close to and shortly before the field maximum. All three regions in the initial distribution are characterized by similar perpendicular momentum of about $p_\perp(t_0) \approx 0.1$ a.u. with a slight increase in $p_\perp$ for higher order LES. This classical analysis confirms that only specific and well-separated parts of the total initial distribution $(t_0, p_\perp(t_0))$ are responsible for the LES islands. Moreover, the analysis readily explains why the LES structure is suppressed in the Coulomb-Volkov approximation. The focusing requires alternating sequences of dominant interactions ("kicks") with the laser field before and after the turning point. Such alternating interaction vertices are absent in the factorized form of Eq. (7) of the CVA final state.

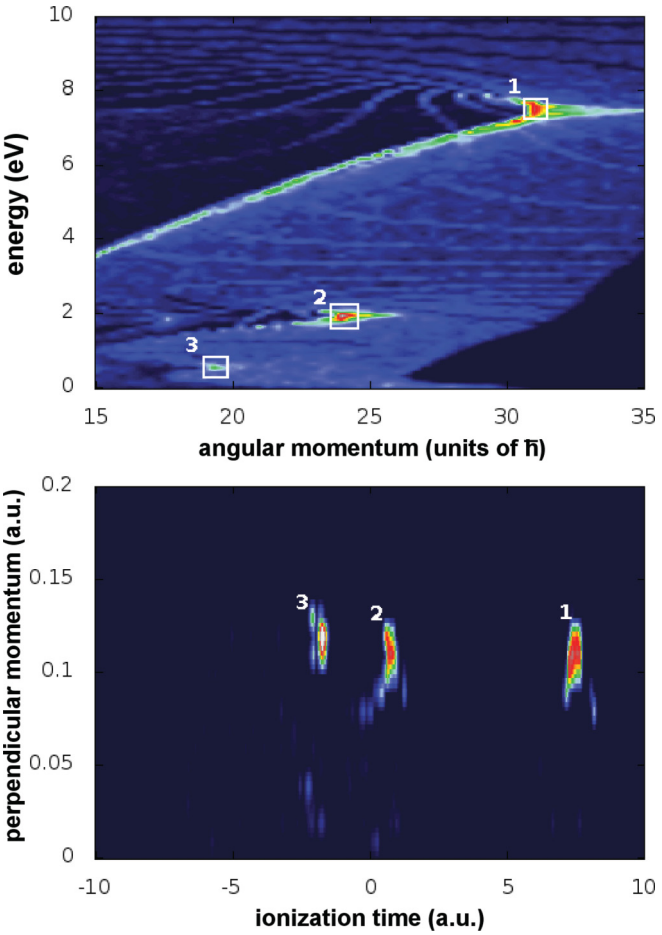

FIG. 8. (Color online) Phase-space mapping of initial states $(t_0, p_{\perp,0})$ onto final states (E, L) for the multiple LES. $\lambda = 3200$ nm, $I = 10^{14}$ W/cm^2, 14 cycles cosine-like pulse, ionization restricted to central half pulse, $p_{\parallel,0} = 0$.

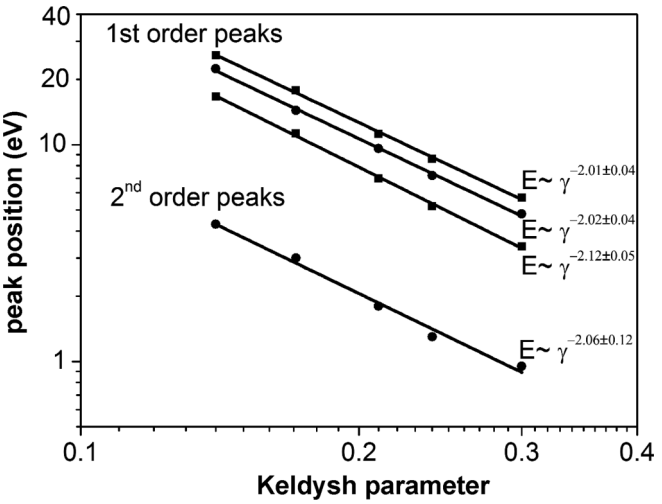

FIG. 9. Scaling of the position of the LES with γ using an eight-cycle laser pulse with fixed peak intensity $I = 10^{14}$ W/cm^2. For the first order LES positions in forward (squares) and backward (circles) directions are plotted separately.

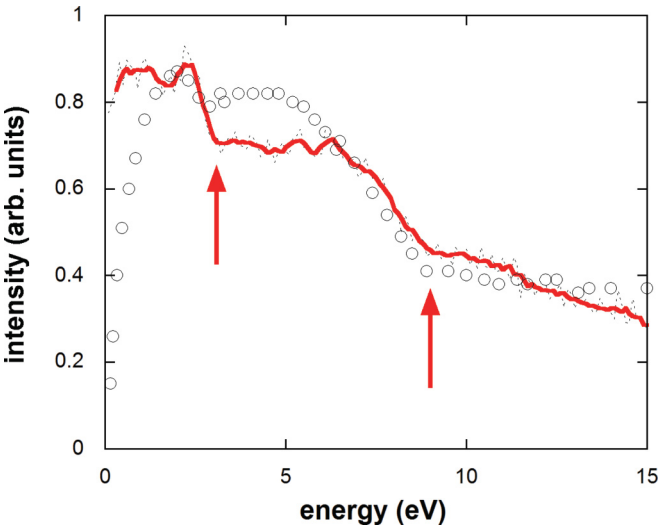

FIG. 10. (Color online) CTMC energy spectra for tunneling ionization (I_p for xenon) interacting with a 3600 nm laser pulse averaged over a Gaussian intensity distribution ($I_{max} = 0.8 \times 10^{14}$ W/cm^2) and averaged over ϕ_{CEP} (red solid line). The total pulse duration was 30 cycles. The spectrum was recorded for 6° opening angle of the electron detector to match the experimental conditions [35], experimental data [6] are shown as open circles. The high-energy cutoffs of the first and second-order LES are marked by arrows.

C. Intensity averaging

Although of considerable conceptual interest, the hierarchy of LES might be difficult to observe due to the strong intensity dependence parametrized here by the variation of the Keldysh parameter γ. The positions of the different LES maxima scale as $E_i \propto \gamma^{-2}$ (Fig. 9). Taking into account averaging over the intensities within a focal volume will considerably broaden the LES peaks towards lower energies and, quite possibly, overshadow high order low-energy structures. The experimentally determined dependence of the high energy cutoff $E_{cut} \propto \gamma^{-1.8\pm0.1}$ [6] is approximately reproduced by our classical simulation when compared with the position of the LES maxima (Fig. 9).

For a more detailed estimate as to the experimental observability of LES, also the effect of the variation of the carrier-envelope phase, in addition to the intensity variation over the focal volume, should be considered. The energy spectrum of emitted electrons averaged over ϕ_{CEP} and a Gaussian intensity profile with maximum intensity $I = 0.8 \times 10^{14}$ W/cm^2, $\lambda = 3600$ nm, and 30 cycles pulse duration have been calculated for the ionization potential of xenon allowing for a comparison with the data reported in Refs. [6,35] (Fig. 10). The sharp LES feature is now smeared out and can only be recognized as a broad feature on top of an approximately exponentially decreasing background. At low energy ($E < 2$ eV) the second-order LES appears. The positions of the high-energy cutoffs for the first and second order LES coincide with the experimental data. The width and the signal to background ratio of the LES, however, are larger in experiment than in the simulation. Further analysis of the averaged LES shows that height and width of the broadened LES scale differently with γ, which may also account for the slight deviation of the experimentally observed $\gamma^{-1.8}$ dependence of the cutoff from the γ^{-2} scaling of the position of the LES maxima.

IV. CONCLUSIONS

The atomic photoionization spectrum generated by short midinfrared laser pulses displays both strong quantum interference effects and classical focusing effects. On the fine scale pronounced intercycle and intracycle interferences appear. The latter are enhanced for larger λ due to the increase of the maximum momentum $k_{max} \sim F_0\lambda$ for two-path interferences. On a larger energy (or momentum) scale, the averaged spectra reveal strong classical focusing effects due to soft rescattering at the atomic (in the present case, Coulomb) potential. The positions and the forward-backward asymmetry of the LES peaks depend on the wavelength, pulse duration, and carrier-envelope phase. The latter may open up the opportunity to monitor ϕ_{CEP} in the low-energy continuum. The LES is absent in the Coulomb-Volkov approximation despite the fact that both the laser field and the Coulomb field are approximately included in the continuum final state. This is due to the lack of alternating interactions of the electron with the laser field and the Coulomb field, an essential ingredient of the soft rescattering mechanism. With increasing λ the energetic position of higher order LES increases with λ^2. However, their visibility may be limited by the averaging over the intensity profile of the laser.

ACKNOWLEDGMENTS

This work was supported by Austrian Science Fund FWF through SFB-ViCoM, SFB NextLite, and project V193-N16 (S.G.). X.M.T. was supported by a Grand-in-Aid for Scientific Research (C24540421) from the Japan Society for the Promotion of Science and the TDSE simulation was carried out at the supercomputer of the HA-PACS project for advanced interdisciplinary computational sciences by exascale computing technology. D.G.A. acknowledges financial support by CONICET, UBA, and ANPCYT of Argentina. K.D. gratefully acknowledges financial support from the Vienna University of Technology. The authors thank Jan-Michael Rost for fruitful discussions on LES.

[1] *Strong Field Laser Physics*, Springer Series in Optical Sciences, edited by T. Brabec, Vol. 134 (Springer, New York, 2009).
[2] L. Keldysh, Zh. Eksp. Teor. Fiz. **47**, 1945 (1964) [Sov. Phys. JETP **6**, 1307 (1965)].
[3] F. H. M. Faisal, J. Phys. B **6**, L89 (1973).
[4] H. R. Reiss, Phys. Rev. A **22**, 1786 (1980).
[5] F. H. M. Faisal, Nat. Phys. **5**, 319 (2009).
[6] C. I. Blaga, F. Catoire, P. Colosimo, G. G. Paulus, H. G. Muller, P. Agostini, and L. F. DiMauro, Nature Phys. **5**, 335 (2009).

[7] T. M. Yan, S. V. Popruzhenko, M. J. J. Vrakking, and D. Bauer, Phys. Rev. Lett. **105**, 253002 (2010).
[8] J. Guo, X.-S. Liu, and Shih-I. Chu, Phys. Rev. A **82**, 023402 (2010).
[9] I. A. Burenkov, A. M. Popov, O. V. Tikhonova, and E. A. Volkova, Laser Phys. Lett. **7**, 409 (2010).
[10] D. A. Telnov and Shih-I. Chu, Phys. Rev. A **83**, 063406 (2011).
[11] W. Quan, Z. Lin, M. Wu, H. Kang, H. Liu, X. Liu, J. Chen, J. Liu, X. T. He, S. G. Chen, H. Xiong, L. Guo, H. Xu, Y. Fu, Y. Cheng, and Z. Z. Xu, Phys. Rev. Lett. **103**, 093001 (2009).
[12] C. Liu and K. Z. Hatsagortsyan, Phys. Rev. Lett. **105**, 113003 (2010).
[13] A. Kästner, U. Saalmann, and J. M. Rost, Phys. Rev. Lett. **108**, 033201 (2012).
[14] C. Lemell, K. I. Dimitriou, X- M. Tong, S. Nagele, D. V. Kartashov, J. Burgdörfer, and S. Gräfe, Phys. Rev. A **85**, 011403(R) (2012).
[15] D. G. Arbó, S. Yoshida, E. Persson, K. I. Dimitriou, and J. Burgdörfer, Phys. Rev. Lett. **96**, 143003 (2006).
[16] T. Popmintchev, M.-C. Chen, D. Popmintchev, P. Arpin, S. Brown, Sk. Alisauskas, G. Andriukaitis, T. Balciunas, O. D. Mücke, A. Pugzlys, A. Baltuska, B. Shim, S. E. Schrauth, A. Gaeta, C. Hernandez-Garcia, L. Plaja, A. Becker, A. Jaron-Becker, M. M. Murnane, and H. C. Kapteyn, Science **336**, 1287 (2012).
[17] X. M. Tong and S. I. Chu, Chem. Phys. **217**, 119 (1997).
[18] X. M. Tong, K. Hino, and N. Toshima, Phys. Rev. A **74**, 031405(R) (2006).
[19] D. P. Dewangan and J. Eichler, Phys. Rep. **247**, 59 (1997).
[20] D. M. Volkov, Z. Phys. **94**, 250 (1935).
[21] D. G. Arbó, J. E. Miraglia, M. S. Gravielle, K. Schiessl, E. Persson, and J. Burgdörfer, Phys. Rev. A **77**, 013401 (2008).
[22] P. B. Corkum, Phys. Rev. Lett. **71**, 1994 (1993).
[23] K. I. Dimitriou, D. G. Arbó, S. Yoshida, E. Persson, and J. Burgdörfer, Phys. Rev. A **70**, 061401(R) (2004).
[24] N. B. Delone and V. P. Krainov, J. Opt. Soc. Am. B **8**, 1207 (1991).
[25] D. G. Arbó, K. L. Ishikawa, K. Schiessl, E. Persson, and J. Burgdörfer, Phys. Rev. A **81**, 021403(R) (2010).
[26] D. G. Arbó, K. L. Ishikawa, K. Schiessl, E. Persson, and J. Burgdörfer, Phys. Rev. A **82**, 043426 (2010).
[27] A. Kästner, U. Saalmann, and J. M. Rost, J. Phys. B **45**, 074011 (2012).
[28] F. B. Dunning, J. J. Mestayer, C. O. Reinhold, S. Yoshida, and J. Burgdörfer, J. Phys. B **42**, 022001 (2009).
[29] C. Liu and K. Z. Hatsagortsyan, J. Phys. B **44**, 095402 (2011).
[30] J. Burgdörfer and J. Gibbons, Phys. Rev. A **42**, 1206 (1990).
[31] L. D. Landau and E. M. Lifschitz, *Lehrbuch der theoretischen Physik*, Vol. 1 (Verlag Harri Deutsch, Thun, 1997).
[32] C. Y. Wu, Y. D. Yang, Y. Q. Liu, Q. H. Gong, M. Y. Wu, X. Liu, X. L. Hao, W. D. Li, X. T. He, and J. Chen, Phys. Rev. Lett. **109**, 043001 (2012).
[33] W. Miller, Adv. Chem. Phys. **25**, 69 (1974).
[34] J. M. Rost, Phys. Rep. **297**, 271 (1998).
[35] P. Colosimo, G. Doumy, C. I. Blaga, J. Wheeler, C. Hauri, F. Catoire, J. Tate, R. Chirla, A. M. March, G. G. Paulus, H. G. Muller, P. Agostini, and L. F. DiMauro, Nat. Phys. **4**, 386 (2008).